THE JOURNAL OF PHYSICAL CHEMISTRY C
A JOURNAL OF THE AMERICAN CHEMICAL SOCIETY

pubs.acs.org/JPCC

Article

Thermodynamics of Sulfur Vacancy Formation in the Chalcogenide Perovskite $BaZrS_3$

Zhenzhu Li* and Aron Walsh

Cite This: *J. Phys. Chem. C* 2025, 129, 19473−19479

Read Online

ACCESS | Metrics & More | Article Recommendations | Supporting Information

ABSTRACT: Chalcogenide perovskites such as $BaZrS_3$ hold potential as promising photovoltaic materials; however, their integration into solar energy devices is currently limited by the high-temperature processing requirements. To explore alternative low-temperature synthesis pathways, we performed an ab initio thermodynamic analysis, highlighting the critical role of sulfur vapor flux, mainly gaseous S_2 and S_8, in driving the synthesis. Our findings reveal that sulfur vapor precursors can provide a thermodynamic driving force $10-10^2$ times stronger than that from traditional solid-state methods. Moreover, we find that sulfur gas composition significantly affects the concentration of sulfur vacancy defects in $BaZrS_3$. In particular, for low-temperature synthesis below 600 °C, gaseous S_2 emerges as the optimal precursor to produce high-quality $BaZrS_3$ with reduced defect concentrations. The thermodynamic trend of sulfur vacancy formation is governed by the evaporative nature of sulfur and is independent of specific synthesis reactions. This conclusion holds broader implications for generic chalcogenide synthesis where sulfur vacancy management is important.

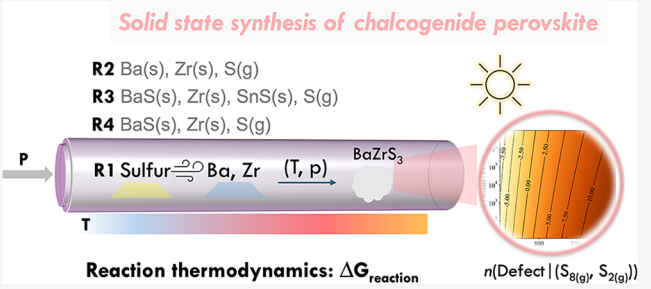

1. INTRODUCTION

As an emerging chalcogenide-based photovoltaic material, the perovskite phase of $BaZrS_3$ has promising photovoltaic properties, such as high photoabsorption coefficient, suitable band gap, and defect tolerance.[1−6] Like many sulfides, the synthesis of $BaZrS_3$ can be tracked back to the 1950s; however, difficulties remained in synthesizing samples that have high crystallinity and uniform film formation.[7] Due to the brittleness of the ionic structure, even with advanced synthesis techniques today, achieving the high crystallinity growth of $BaZrS_3$ film remains difficult, resulting in the predominant study of powder samples.[8−11] The inhomogeneous grain size and distribution and poor crystallinity of powder samples are detrimental to their photovoltaic efficiency by leading to serious interfacial contact and charge transport issues, severely hindering their application in photovoltaic devices.

In addition, the high synthesis temperature poses another challenge when integrating $BaZrS_3$ to photovoltaic devices, due to the high temperature of annealing required to improve the crystalline quality of the materials, which is a process for device fabrication to activate dopants, repair defects, and enhance electrical and optical properties. Thereby, comprehensive growth thermodynamics is essential here to provide insights into directing the design of $BaZrS_3$ synthesis conditions.

Another aspect for achieving high-quality samples is the mitigation or reduction of defects. A common defect found in chalcogenides is anion deficiency,[12,13] attributed to the lower formation energy of V_S^{2+} compared with other defect species.[14] This defect formation behavior is also closely tied to the thermodynamic growth conditions, such as the partial pressures (p) of gaseous precursors and temperature (T), which influence the formation of defect species by altering their chemical potentials. Moreover, the complex sulfur chemistry in the vapor phase would exacerbate the intricacy of this interplay, particularly concerning sulfur-related defects.[15−17]

To address these challenges, we calculate the thermodynamics of $BaZrS_3$ growth via various synthesis routes, while also examining their impact on defect formation, particularly in relation to the sulfur chemistry in the vapor phase.

1.1. Routes for Synthesizing $BaZrS_3$.

A range of strategies exist for synthesizing solid-state materials, such as (1) solid-state reactions, usually an elevated temperature is required, (2) gas-phase reactions with flux, (3) hydrothermal reactions, and (4) intercalation or coordination reactions.[15] The explored synthesis routes to prepare $BaZrS_3$ mainly focus on the solid-state and gas-phase reaction strategies,[18] with a recent progress on using hydrothermal reaction[19] or in a liquid-assisted way,[20−22] which are not considered in this work due to the complexity of the solution. In the present work, we

Received: February 5, 2025
Revised: October 12, 2025
Accepted: October 13, 2025
Published: October 22, 2025

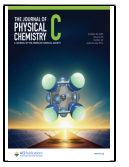

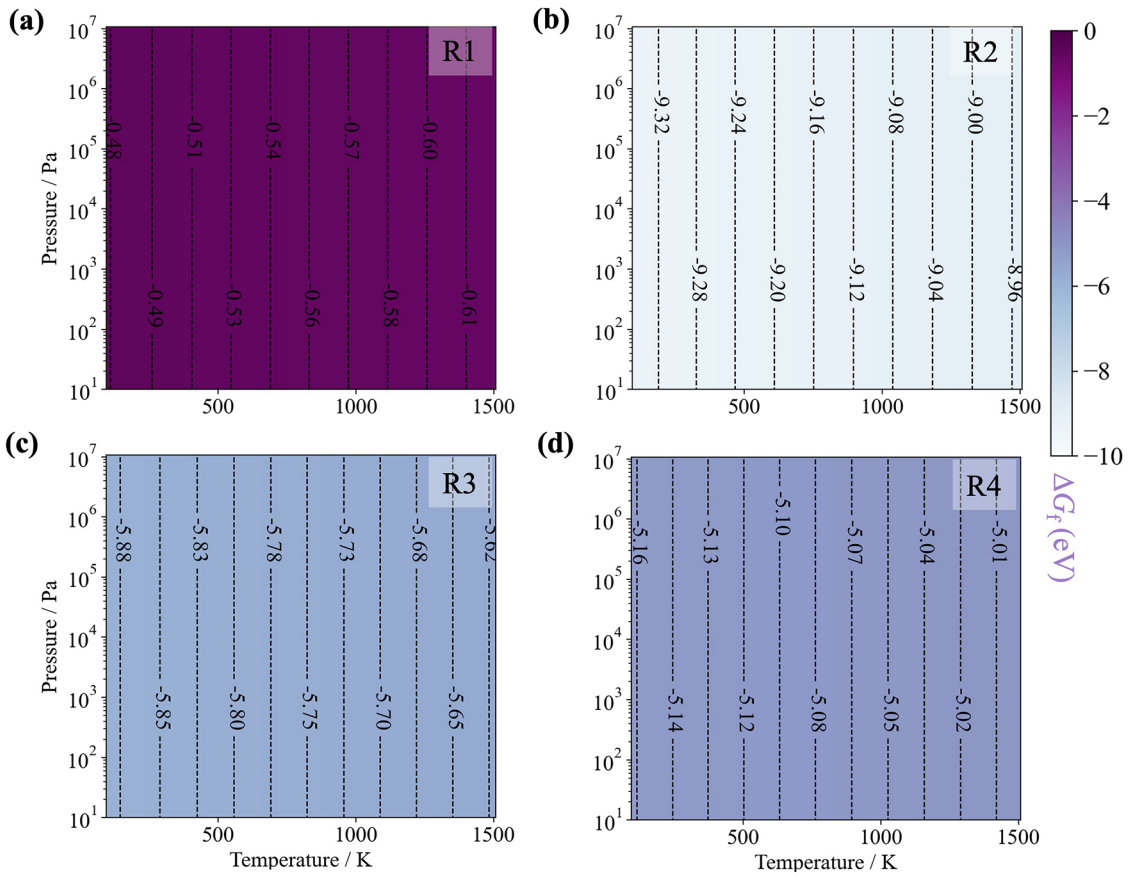

Figure 1. Reaction free energies (eV/f.u.) for synthesizing $BaZrS_3$ via Reactions 1−4 (a−d) under an operating window with temperature ranging from 0 to 1000 K and pressure from 0 to 10^7 Pa, suppose that S remains solid across the entire synthesis window. R1−R4 denote the four reactions.

only considered gaseous sulfur as the precursor. For reactions involving $BaZrO_3$ and H_2S or CS_2, the reaction free energies can, in principle, be calculated, as the expected products are $BaZrS_3$ and H_2O or CO_2. We have confirmed that the necessary thermodynamic data for these gaseous species are available in the NIST-JANAF Thermochemical Tables. This represents an interesting direction for further investigation, which we plan to pursue in our follow-up research. Here, four representative reactions will be discussed, including one solid-state reaction

$$BaS(s) + ZrS_2(s) \xrightarrow{800-1000\ ^\circ C} BaZrS_3(s) \quad (R1)$$

and three gas-phase reactions.

$$Ba(s) + Zr(s) + 3\ S(g) \rightarrow BaZrS_3(s) \quad (R2)$$

$$3\ BaS(s) + Zr(s) + SnS(s) + 3\ S(g) \xrightarrow{600\ ^\circ C} BaZrS_3(s) + Ba_2SnS_4(s) \quad (R3)$$

$$BaS(s) + Zr(s) + 2\ S(g) \xrightarrow{600\ ^\circ C} BaZrS_3(s) \quad (R4)$$

Some of these reactions have been used for synthesizing chalcogenide perovskites.[4,23,24] Due to the high chemical reactivity of Ba, Reaction 2 is an elemental reaction that requires meticulous control. In these reactions, high temperatures are usually required. For example, due to the strong stability of BaS and ZrS_2, the solid-state reactions with metal sulfide binaries necessitate a furnace heated to near 1000 °C;[3] in contrast, by introducing gaseous sulfur from volatile sulfur precursors, the reaction temperatures could be lowered down to 600 °C.[24] A recent work focused on the thermodynamic stability of $BaZrS_3$, BaS_x, and ZrS_x using Reactions 1 and 2 found that both reactions were sensitive to sulfur allotropes and the extent of allotrope mixing.[25] Nevertheless, the full thermodynamic picture necessary to evaluate the $BaZrS_3$ synthesis window across the four reactions, as well as the defect formation thermodynamics, remains to be addressed.

2. COMPUTATIONAL METHODS

The thermodynamic analysis required total energies and phonon properties for a range of solids ($BaZrS_3$, Ba, Zr, S, BaS, ZrS_2, SnS, and Ba_2SnS_4) and gas phases (S_8 and S_2). The associated first-principles calculations were performed using VASP[26,27] with the standard frozen-core projector augmented-wave method.[28,29] The cutoff energy for the plane wave basis functions was set to 700 eV. The generalized gradient approximation[30] of the Perdew−Burke−Ernzerhof functional for solids (PBEsol)[31] was used for the description of exchange and correlation. We used a 7 × 7 × 7 k-point mesh for structural relaxation until all atoms were relaxed with Hellmann−Feynman forces below 0.01 eV/Å. The role of spin−orbit coupling (SOC) is not considered in this work.

Phonon calculations were computed with the PHONOPY[32] using the finite displacement method to extract the heat capacity and vibrational entropy of the solid phases. The sulfur vacancy defect formation energy ($\Delta H_{D,q}$) is determined with the Heyd−Scuseria−Ernzerhof (HSE06) hybrid functional[33−35] again using VASP, and the calculations were conducted

https://doi.org/10.1021/acs.jpcc.5c00828
J. Phys. Chem. C 2025, 129, 19473−19479

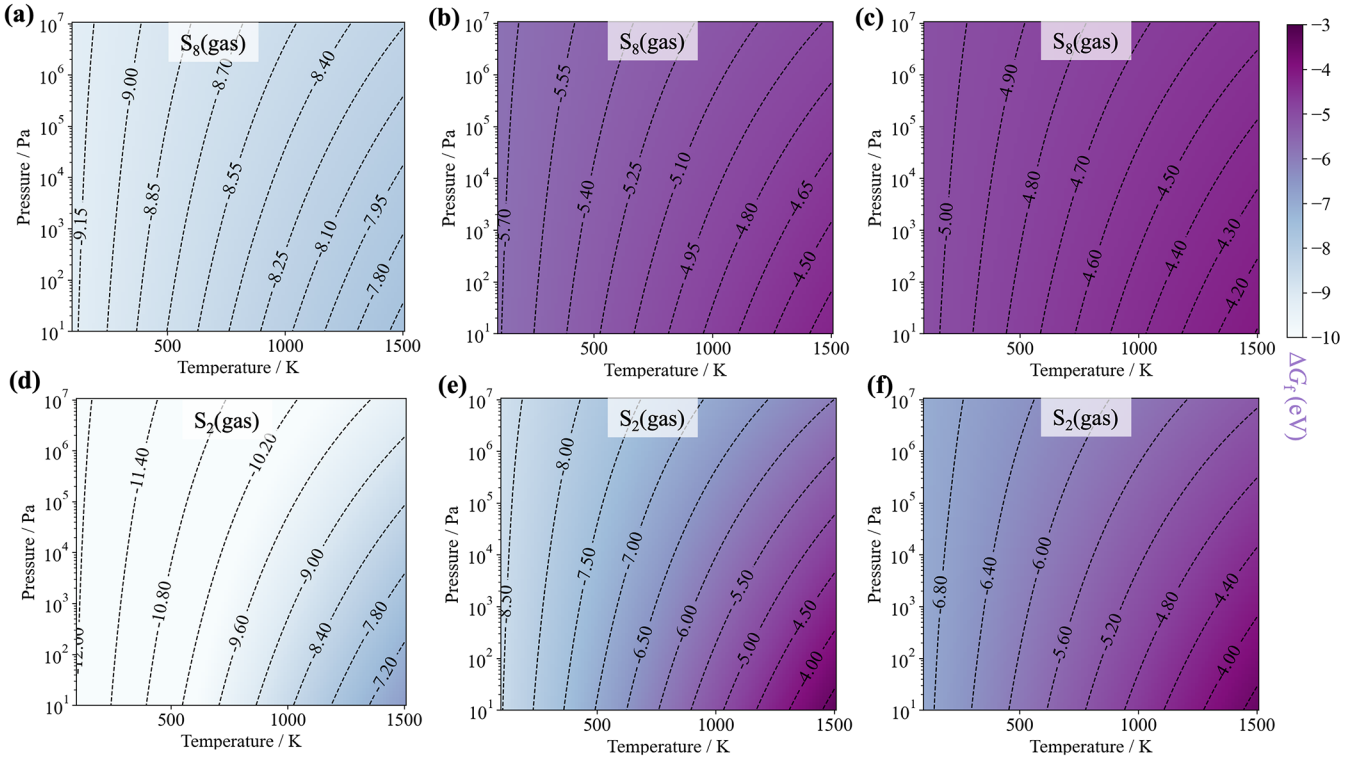

Figure 2. Reaction free energies for synthesizing $BaZrS_3$ via Reactions 2−4 considering an operating window spanning temperature from 0 to 1000 K and S partial pressure up to 10^7 Pa under the evaporated sulfur picture. (a, d) Reaction 2. (b, e) Reaction 3. (c, f) Reaction 4.

following the SHAKENBREAK[36,37] workflow to ensure the ground state configurations of defects. The change of chemical potentials of gaseous S_8 and S_2 was treated separately and calculated with PBEsol functional and then combined with $\Delta H_{D,q}$ to determine the concentration of V_S^{2+} defect. Full calculation details can be found in our GitHub repository.

3. RESULTS AND DISCUSSION

3.1. Ab Initio Thermodynamics of Synthesizing $BaZrS_3$. First-principles calculations offer a powerful tool for accurately predicting the thermodynamics for the synthesis of solid-state materials.[38] Due to the evaporating nature of sulfur, the growth temperature and its partial pressure will influence the thermodynamic driving force for these synthesis reactions. However, energy minimization with density functional theory (DFT) is based solely on the internal energy and does not account directly for any lattice vibrations or the effect of gaseous pressure.[39,40]

Under the assumption of ideal materials, for species i involved in the reaction, by adding its zero-point vibrational energy E_i^{ZP} to the DFT computed energy E_i^{DFT}, we can obtain its Gibbs free energy at zero temperature and zero pressure (G_i^0), and per unit G_i^0 is thermodynamically equivalent to its chemical potential μ_i^0. Hence, we have $\mu_i^0 = G_i^0 = E_i^{DFT} + E_i^{ZP}$. For species i at given reaction conditions, the chemical potential is $\mu_i(T, p)$ defined by eq 1, where μ_i^θ is the reference chemical potential under standard conditions of 298.15 K and 1 bar. $[H_i^\theta - H_i^0]$ is the standard enthalpy and $(TS)^\theta = 298.15\ K \times S^\theta$ is available from the literature data.[39,41]

$$\mu_i(T, p) = E_i^{DFT} + E_i^{ZP} + [\mu_i(T, p) - \mu_i^\theta] + [H_i^\theta - H_i^0] - (TS)^\theta \quad (1)$$

For the incompressible solid phase, due to the relatively high bulk modulus of $BaZrS_3$ (75 GPa),[42] the influence of pressure and thermal expansion is neglected. Under an absolute pressure P, the chemical potential is calculated by

$$\mu_i(T, p_i) = E^{DFT} + E^{ZP} + [H_i^\theta - H_i^0] + \int_{T^\theta}^{T} C_v dT + PV - TS(T, p_i^\theta) \quad (2)$$

while for ideal gases,

$$\mu_i(T, p_i) = E^{DFT} + E^{ZP} + [H_i^\theta - H_i^0] + \int_{T^\theta}^{T} C_p dT + RT \ln[p_i/p_i^\theta] - TS(T, p_i^\theta) \quad (3)$$

Aside from the incompressible solid and ideal gas assumption, the calculation of $\mu_i(T, p)$ requires some data from literature and lattice dynamics calculations. Finally, the reaction free energy ΔG_f could be calculated from eq 4, where a negative sign of ΔG_f denotes the reaction toward the product end, and the more negative the value, the higher the driving force for the reaction to occur.

$$\Delta G_f = \Delta\mu = \sum_i \mu_{products,i} - \sum_i \mu_{reactants,i} \quad (4)$$

In Figure 1, the reaction free energies (ΔG_f) of synthesizing $BaZrS_3$ via Reactions 1−4 under operating window with temperature ranging from 0 to 1000 K and pressure from 0 to 10^7 Pa are presented. When treating all of the solids as incompressible and treating S as a solid at all temperatures, all four synthesis routes are favored toward the product end driven by the change of free energies.

Reaction 1, initiated with the metal binaries, exhibited the smallest change of Gibbs free energy in the range of −0.48 to

https://doi.org/10.1021/acs.jpcc.5c00828
J. Phys. Chem. C 2025, 129, 19473−19479

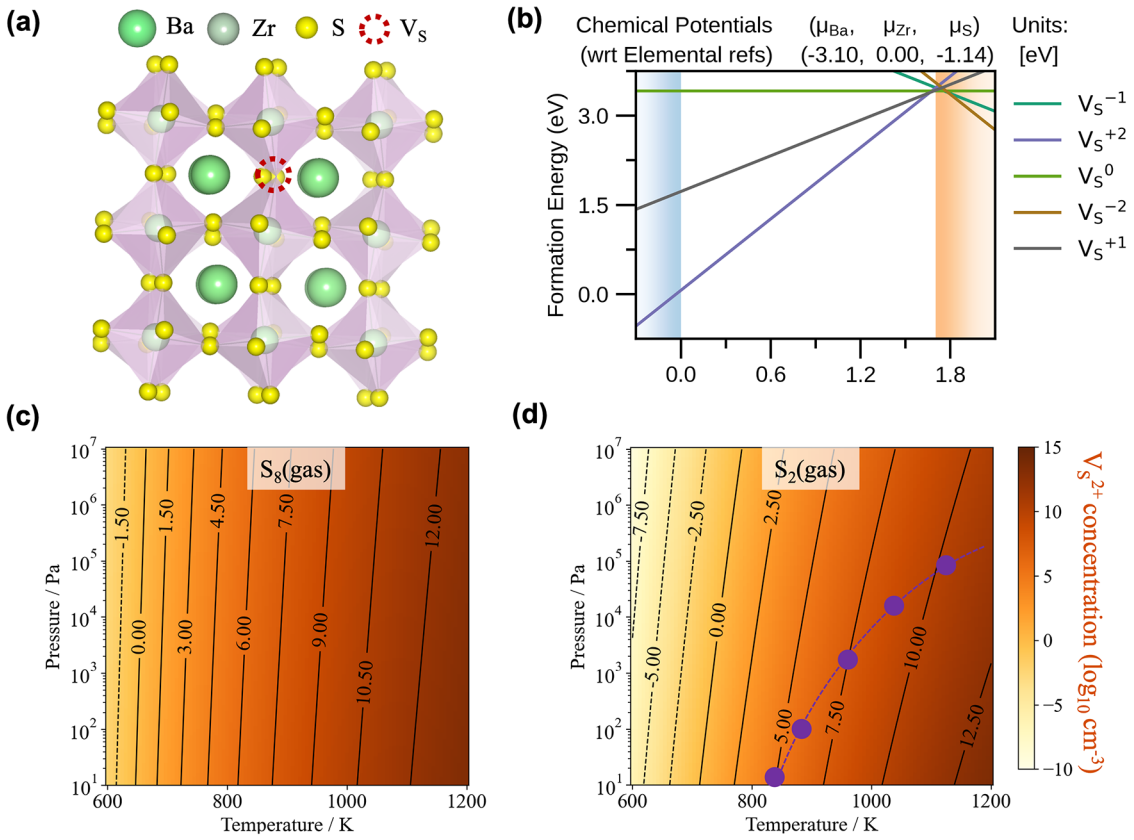

Figure 3. (a) Sulfur vacancy in a $BaZrS_3$ crystal and (b) formation energy in five charge states as a function of the Fermi level under S-poor conditions. Predicted defect concentration for equilibrium with respect to (c) S_8 and (d) S_2 vapor as a function of temperature and pressure. The purple dashed line on (d) denotes the boundary when the defect concentration is equal using either solid-state α-S(s) or S_2(g) as the growth precursor.

−0.60 eV/f.u., indicating a comparatively lower thermodynamic driving force toward product formation. In Reaction 2, the energy change is as much as −9 eV/f.u., reflecting the high reactivity of the elemental substances Ba, Zr, and S. The free energies of Reactions 3 and 4 occupy intermediate positions in the energy spectrum, showing the effect of reactant choice. For instance, in Reaction 3, when modulated with a mixed sulfur source derived from SnS and S, the driving force of reaction was approximately −5.7 eV/f.u. and the reaction temperature was lowered to 600 °C experimentally;[24] in Reaction 4, employing the inert metal binary BaS and elemental Zr and S as the reactants, the change of free energy is 0.6 eV/f.u. smaller than that in Reaction 3, and reported a similar reaction temperature of 600 °C.[4] Nonetheless, regardless of the reaction pathways, due to the high stability of $BaZrS_3$, the formation of the desired product is favored. Since all reactions are thermodynamically favorable at all temperatures, the temperature is mainly needed to overcome kinetic barriers. Reaction free energies and activation energies can be inversely correlated, so a larger thermodynamic driving force implies a lower kinetic barrier.[43]

In practical experiments, the volatile nature of sulfur will drive the thermodynamic free energy landscape away from all solid-state reactions.[17] In the gas phase, the evaporated sulfur can manifest as a mixture of S_8, S_7, S_6, and so forth, with their relative mixing ratio fluctuating in response to the growth temperature and sulfur partial pressure, introducing an additional layer of complexity to the thermodynamic evaluation on the synthesis of $BaZrS_3$. S_8 and S_2 can serve as suitable approximations to the sulfur gas-phase components across the relevant temperature range.[17] At lower temperatures, bulk sulfur evaporates into the dominating form of S_8 initially, while as growth temperatures surpass a theoretical 400 °C, S_2 emerges as the primary form of sulfur vapor. The change in S vapor composition will influence its chemical potential and, in turn, the growth of $BaZrS_3$.

The thermodynamic landscapes, with a specific focus on evaporated S_8 and S_2 gases across Reactions 2−4 are shown in Figure 2. In the case of gases, the term $\int_{T^\theta}^{T} C_p\, dT + RT \ln [p_i/p_i^\theta]$ in the chemical potential expression (eq 3) dominates the growth driving force. Taking Reaction 2 with elemental substances Ba, Zr, and S as an example, under identical growth conditions (T, p), if all sulfur was to evaporate as gaseous S_8, the reaction ΔG_f was increased by approximately 0.15−1 eV/f.u. across the entire growth window, consequently retarding the driving force for forward reaction. Conversely, if all sulfur was transformed into gaseous S_2, the reaction would be significantly propelled toward the product end by providing an additional reaction free energy change from 2.7 to 0 eV/f.u. when the growth temperature is increased up to 820 K. Interestingly, with temperature further increasing, the reaction ΔG_f starts to increase with a magnitude from 0 to 1.8 eV/f.u. across the remaining growth window. This originates from the fact that it crosses the "equivalence" boundary where $\mu(\alpha\text{−S}) = \mu(S_2)$, which will be addressed later.

Similar trends are observed for Reaction 3 initiated with BaS, Zr, SnS, and S, and Reaction 4 beginning with BaS, Zr, and S. It is worth noting that although SnS is expected to decompose

https://doi.org/10.1021/acs.jpcc.5c00828
J. Phys. Chem. C 2025, 129, 19473−19479

or sublimate across the growth windows, it is treated as an incompressible solid here. Nonetheless, the inclusion of SnS in the reaction stoichiometry plays a crucial role in promoting a more uniform growth of $BaZrS_3$,[24] compared with samples obtained from Reaction 4.[4] In addition to its role in suppressing oxidation and being thermally removable, the presence of SnS introduces a competing factor for tuning the partial pressure of S in the gas phase, thereby offering a new design strategy for lowering the growth temperatures of $BaZrS_3$. Also, as shown in Figure 2, for the thin-film growth of $BaZrS_3$ in a vacuum chamber, when the partial pressures of sulfur are much lower, for example, 10^1 Pa, the reaction still favors the product end thermodynamically while the reaction driving force (ΔG_f) for each reaction temperature will be smaller than that under higher sulfur partial pressure. In this case, temperature plays a critical role in compensating for the loss of reaction driving forces.

In general, the composition of sulfur vapor alters the growth thermodynamics, with gaseous S_8 generally retarding reactions, while gaseous S_2 propels them forward. Therefore, the key to achieving a lower temperature synthesis lies in how to prioritize the presence of S_2 as the primary gaseous component. This can be achieved at elevated temperatures through direct sublimation of α-S or from the breakdown of S_8 (see Figure S3). We calculated these two reactions following the procedures introduced in ref 17, under the assumption that both α-S and S_8 can be decomposed into various sulfur species including S_2. Alternatively, a separate "cracking" stage can be used to feed in activated S_2 directly as a reactant for synthesis.

3.2. Control of V_S^{2+} Defect Formation. One crucial aspect in growing high-quality $BaZrS_3$ for optoelectronic applications is defect control. In $BaZrS_3$, there are more than one hundred distinct types of defects that might present, including vacancies, interstitials, and antisites with different charge states (analysis performed via DOPED[44]). The formation energies for some of these have been reported before without detailed consideration of the growth environments.[3,14]

We focus on the important case of the sulfur vacancy, which has the potential to act as an electron trap and nonradiative recombination center in metal sulfide semiconductors.[45,46] Ref 46 presents a modeling study based on 0 K DFT simulations that identifies a potential deep transition-level defect−sulfur interstitials. Our work agrees with their conclusion that sulfur vacancies exhibit shallower defect transition levels at 0 K. Furthermore, we extend this understanding by investigating the defect behavior under finite temperature and pressure growth conditions. The formation energy is calculated using the standard formalism for charged defects in solids,

$$\Delta H_{D,q}(E_F, \mu) = [E_{D,q} - E_H] + \sum_i n_i\mu_i + qE_F + E_{corr} \quad (5)$$

where the electronic and chemical potentials for forming a defect D in charge state q are determined by E_F and μ, respectively. Corrections for finite-size effects (E_{corr}) are implemented following the approach of Kumagai and Oba.[47]

As shown in Figure 3b, among V_S^{2+}, V_S^{1+}, V_S^0, V_S^{1-}, and V_S^{2-}, V_S^{2+} has the lowest formation energy. We assume an intrinsic semiconductor where the equilibrium Fermi level is placed in the center of the band gap. Under the S-deficient conditions, the formation energy of V_S^{2+} is about 1.5 eV (Figure 3b), which can be tuned by the sulfur chemical potentials. Under S-rich conditions, the formation energy is increased to around 3 eV (Figure S2). It is important to note that lower defect formation energy corresponds to higher equilibrium defect concentrations. Therefore, our focus is on manipulating the S-deficient conditions to optimize the defect population.

From Figure 3c,d, we can find that higher growth temperatures consistently result in higher defect concentrations. Pressure poses minimal effect on defect formation in incompressive solid-state reactions when using α-S as the growth precursor with the highest V_S^{2+} concentration at the level of 10^{11} cm^{-3}, while gaseous S_8 leads to higher defect concentrations across the entire growth window compared with reactions with α-S, showing the highest V_S^{2+} concentration over 10^{12} cm^{-3}. Meanwhile, using pure gaseous S_2 as the growth precursor, as shown in Figure 3d, the boundary is delineated denoting the growth conditions where the defect concentration is equivalent when using either solid-state α-S or S_2 gas as the growth precursors. To the right side of the boundary, where the growth temperature exceeds 820 K and the pressure is below 1 bar, solid-state α-S is preferred for reducing the defect concentration. However, under most of the growth windows below 820 K, gaseous S_2 proves favorable for growing high-quality crystals, with defect concentration being substantially lower than using other sulfur sources.

It is worth noting that the absolute defect concentrations of V_S^{2+} in $BaZrS_3$ under all conditions are low because of the high defect formation energy. However, the comparative orders of magnitude change in defect concentration are significant. A reduction of one to two orders in defect concentration can have a profound impact on material properties. This influence is general and arises from the difference in chemical potential

$$\Delta\mu_i(T, p_i)(S_s \rightarrow S_g) = \mu_i(T, p_i)_{(S_g)} - \mu_i(T, p_i)_{(S_s)} \quad (6)$$

which changes the V_S formation energy (eq 5).

In consensus with other modeling and experimental works,[3,14,46,48] $BaZrS_3$ is a defect-tolerant material for efficient solar energy conversion, with shallow defect transition levels for almost all types of vacancies, interstitials, and antisite defects; our results also agree with the experimental observation that as-grown $BaZrS_3$ is intrinsically n-type, due to the ease of formation of sulfur vacancy. Also recently presented in ref 46, under the S-rich condition, sulfur interstitials can be potential nonradiative recombination centers in this material.

The density of V_S defects demonstrates a correlation with the annealing temperature and duration. This observation falls into a family of thermodynamic relations governing defect formation with gaseous precursors, such as O_2 used in metal oxide synthesis, where the formation energies of intrinsic point defects are strongly coupled to the partial pressure of oxygen.[49,50]

4. CONCLUSIONS

Through our ab initio thermodynamic calculations on different $BaZrS_3$ synthesis strategies, the reaction Gibbs free energy results reveal that synthesis is favorable over a large temperature and pressure range. This outcome persists even when initiating the reaction with stable metal binaries BaS and ZrS_2 as the growth precursors. Therefore, the feasibility of low-temperature synthesis is primarily constrained by the reactivity of precursors. In the context of gas flux-assisted synthesis, we have highlighted that S_2 proves beneficial for growing high-quality samples compared with other states of sulfur. This also

https://doi.org/10.1021/acs.jpcc.5c00828
J. Phys. Chem. C 2025, 129, 19473−19479

carries through to the control of equilibrium sulfur vacancy concentrations. Additionally, there is a recent trend in liquid-assisted growth of $BaZrS_3$ to further lower the reaction temperatures, which we perceive to be somewhat analogous to the gas flux-assisted synthesis, albeit more complex due to the difficulty in describing the activity of reaction precursors in the solution.

■ ASSOCIATED CONTENT

Supporting Information

The Supporting Information is available free of charge at https://pubs.acs.org/doi/10.1021/acs.jpcc.5c00828.

Figure S1: Chemical potential and phase diagram of Ba, Zr, S; Figure S2: Sulfur vacancy formation energy as a function of the Fermi level under different sulfur chemical potentials. Figure S3: Reaction free energies for alpha sulfur evaporating into the gaseous (a) S_8, (c) S_2, and (b) gaseous S_8 transforming to S_2 (PDF)

■ AUTHOR INFORMATION

Corresponding Author

Zhenzhu Li − *Department of Materials, Imperial College London, London SW7 2AZ, U.K.; Imperial-X, Imperial College London, London W12 7SL, U.K.;* orcid.org/0000-0002-6669-563X; Email: zhenzhu.li@imperial.ac.uk

Author

Aron Walsh − *Department of Materials, Imperial College London, London SW7 2AZ, U.K.;* orcid.org/0000-0001-5460-7033

Complete contact information is available at: https://pubs.acs.org/10.1021/acs.jpcc.5c00828

Notes

The authors declare no competing financial interest.

■ ACKNOWLEDGMENTS

We acknowledge the discussion with Kasper Tolborg in the finalization stages of the project. We are grateful to the UK Materials and Molecular Modelling Hub for computational resources, which is partially funded by EPSRC (EP/P020194/1). Via our membership of the UK's HPC Materials Chemistry Consortium, which is funded by EPSRC (EP/L000202, EP/R029431), this work used the ARCHER UK National Supercomputing Service. This work was supported by the EPSRC project EP/X037754/1 and the Eric and Wendy Schmidt AI in Science Postdoctoral Fellowship, a Schmidt Sciences program.

■ REFERENCES

(1) Bennett, J. W.; Grinberg, I.; Rappe, A. M. Effect of substituting of S for O: The sulfide perovskite $BaZrS_3$ investigated with density functional theory. *Phys. Rev. B* **2009**, *79*, No. 235115.

(2) Sun, Y.-Y.; Agiorgousis, M. L.; Zhang, P.; Zhang, S. Chalcogenide Perovskites for Photovoltaics. *Nano Lett.* **2015**, *15*, 581−585.

(3) Meng, W.; Saparov, B.; Hong, F.; Wang, J.; Mitzi, D. B.; Yan, Y. Alloying and Defect Control within Chalcogenide Perovskites for Optimized Photovoltaic Application. *Chem. Mater.* **2016**, *28*, 821−829.

(4) Niu, S.; Huyan, H.; Liu, Y.; Yeung, M.; Ye, K.; Blankemeier, L.; Orvis, T.; Sarkar, D.; Singh, D. J.; Kapadia, R.; Ravichandran, J. Bandgap Control via Structural and Chemical Tuning of Transition Metal Perovskite Chalcogenides. *Adv. Mater.* **2017**, *29*, No. 1604733.

(5) Nishigaki, Y.; Nagai, T.; Nishiwaki, M.; Aizawa, T.; Kozawa, M.; Hanzawa, K.; Kato, Y.; Sai, H.; Hiramatsu, H.; Hosono, H.; Fujiwara, H. Extraordinary Strong Band-Edge Absorption in Distorted Chalcogenide Perovskites. *Sol. RRL* **2020**, *4*, No. 1900555.

(6) Tiwari, D.; Hutter, O. S.; Longo, G. Chalcogenide perovskites for photovoltaics: current status and prospects. *J. Phys.: Energy* **2021**, *3*, No. 034010.

(7) Clearfield, A. The synthesis and crystal structures of some alkaline earth titanium and zirconium sulfides. *Acta Crystallogr.* **1963**, *16*, 135−142.

(8) Comparotto, C.; Davydova, A.; Ericson, T.; Riekehr, L.; Moro, M. V.; Kubart, T.; Scragg, J. Chalcogenide Perovskite BaZrS3: Thin Film Growth by Sputtering and Rapid Thermal Processing. *ACS Appl. Energy Mater.* **2020**, *3*, 2762−2770.

(9) Wei, X.; Hui, H.; Perera, S.; Sheng, A.; Watson, D. F.; Sun, Y.-Y.; Jia, Q.; Zhang, S.; Zeng, H. Ti-Alloying of BaZrS3 Chalcogenide Perovskite for Photovoltaics. *ACS Omega* **2020**, *5*, 18579−18583.

(10) Ravi, V. K.; Yu, S. H.; Rajput, P. K.; Nayak, C.; Bhattacharyya, D.; Chung, D. S.; Nag, A. Colloidal BaZrS3 chalcogenide perovskite nanocrystals for thin film device fabrication. *Nanoscale* **2021**, *13*, 1616−1623.

(11) Wei, X.; Hui, H.; Zhao, C.; Deng, C.; Han, M.; Yu, Z.; Sheng, A.; Roy, P.; Chen, A.; Lin, J.; et al. Realization of BaZrS3 chalcogenide perovskite thin films for optoelectronics. *Nano Energy* **2020**, *68*, No. 104317.

(12) Guo, Y.; Liu, D.; Robertson, J. Chalcogen vacancies in monolayer transition metal dichalcogenides and Fermi level pinning at contacts. *Appl. Phys. Lett.* **2015**, *106*, No. 173106.

(13) Maiti, A.; Chatterjee, S.; Pal, A. J. Sulfur-Vacancy Passivation in Solution-Processed Sb2S3 Thin Films: Influence on Photovoltaic Interfaces. *ACS Appl. Energy Mater.* **2020**, *3*, 810−821.

(14) Wu, X.; Gao, W.; Chai, J.; Ming, C.; Chen, M.; Zeng, H.; Zhang, P.; Zhang, S.; Sun, Y.-Y. Defect tolerance in chalcogenide perovskite photovoltaic material BaZrS3. *Sci. China Mater.* **2021**, *64*, 2976−2986.

(15) Stein, A.; Keller, S. W.; Mallouk, T. E. Turning Down the Heat: Design and Mechanism in Solid-State Synthesis. *Science* **1993**, *259*, 1558−1564.

(16) Fedyaeva, M.; Lepeshkin, S.; Oganov, A. R. Stability of sulfur molecules and insights into sulfur allotropy. *Phys. Chem. Chem. Phys.* **2023**, *25*, 9294−9299.

(17) Jackson, A. J.; Tiana, D.; Walsh, A. A universal chemical potential for sulfur vapours. *Chem. Sci.* **2016**, *7*, 1082−1092.

(18) Ramanandan, S. P.; Giunto, A.; Stutz, E. Z.; Reynier, B.; Lefevre, I. T. F. M.; Rusu, M.; Schorr, S.; Unold, T.; Fontcuberta I Morral, A.; Morral, A. F. I.; Márquez, J. A. Understanding the growth mechanism of BaZrS3 chalcogenide perovskite thin films from sulfurized oxide precursors. *J. Phys.: Energy* **2023**, *5*, No. 014013.

(19) Yang, R.; Jess, A. D.; Fai, C.; Hages, C. J. Low-Temperature, Solution-Based Synthesis of Luminescent Chalcogenide Perovskite BaZrS3 Nanoparticles. *J. Am. Chem. Soc.* **2022**, *144*, 15928−15931.

(20) Yang, R.; Nelson, J.; Fai, C.; Yetkin, H. A.; Werner, C.; Tervil, M.; Jess, A. D.; Dale, P. J.; Hages, C. J. A Low-Temperature Growth Mechanism for Chalcogenide Perovskites. *Chem. Mater.* **2023**, *35*, 4743−4750.

(21) Vincent, K. C.; Agarwal, S.; Turnley, J. W.; Agrawal, R. Liquid Flux-Assisted Mechanism for Modest Temperature Synthesis of Large-Grain BaZrS3 and BaHfS3 Chalcogenide Perovskites. *Adv. Energy Sustainability Res.* **2023**, *4*, No. 2300010.

(22) Pradhan, A. A.; Uible, M. C.; Agarwal, S.; Turnley, J. W.; Khandelwal, S.; Peterson, J. M.; Blach, D. D.; Swope, R. N.; Huang, L.; Bart, S. C.; Agrawal, R. Synthesis of BaZrS3 and BaHfS3 Chalcogenide Perovskite Films Using Single-Phase Molecular Precursors at Moderate Temperatures. *Angew. Chem., Int. Ed.* **2023**, *62*, No. e202301049.

(23) Hahn, H.; Mutschke, U. Untersuchungen über ternäre Chalkogenide. XI. Versuche zur Darstellung von Thioperowskiten. *Z. Anorg. Allg. Chem.* **1957**, *288*, 269−278.
(24) Comparotto, C.; Ström, P.; Donzel-Gargand, O.; Kubart, T.; Scragg, J. J. S. Synthesis of BaZrS3 Perovskite Thin Films at a Moderate Temperature on Conductive Substrates. *ACS Appl. Energy Mater.* **2022**, *5*, 6335−6343.
(25) Kayastha, P.; Longo, G.; Whalley, L. D. A First-Principles Thermodynamic Model for the Ba-Zr-S System in Equilibrium with Sulfur Vapor. *ACS Appl. Energy Mater.* **2024**, *7*, 11326−11333.
(26) Kresse, G.; Hafner, J. Ab initio molecular dynamics for liquid metals. *Phys. Rev. B* **1993**, *47*, 558−561.
(27) Kresse, G.; Furthmüller, J. Efficient iterative schemes for ab initio total-energy calculations using a plane-wave basis set. *Phys. Rev. B* **1996**, *54*, 11169−11186.
(28) Blöchl, P. E. Projector augmented-wave method. *Phys. Rev. B* **1994**, *50*, 17953−17979.
(29) Kresse, G.; Joubert, D. From ultrasoft pseudopotentials to the projector augmented-wave method. *Phys. Rev. B* **1999**, *59*, 1758−1775.
(30) Perdew, J. P.; Burke, K.; Ernzerhof, M. Generalized gradient approximation made simple. *Phys. Rev. Lett.* **1996**, *77*, No. 3865.
(31) Csonka, G. I.; Perdew, J. P.; Ruzsinszky, A.; Philipsen, P. H. T.; Lebègue, S.; Paier, J.; Vydrov, O. A.; Ángyán, J. G. Assessing the performance of recent density functionals for bulk solids. *Phys. Rev. B* **2009**, *79*, No. 155107.
(32) Togo, A.; Chaput, L.; Tadano, T.; Tanaka, I. Implementation strategies in phonopy and phono3py. *J. Phys.: Condens. Matter* **2023**, *35*, No. 353001.
(33) Heyd, J.; Scuseria, G. E.; Ernzerhof, M. Hybrid functionals based on a screened Coulomb potential. *J. Chem. Phys.* **2003**, *118*, 8207−8215.
(34) Heyd, J.; Scuseria, G. E.; Ernzerhof, M. Erratum: "Hybrid functionals based on a screened Coulomb potential" [J. Chem. Phys. 118, 8207 (2003)]. *J. Chem. Phys.* **2006**, *124*, No. 219906.
(35) Heyd, J.; Scuseria, G. E. Efficient hybrid density functional calculations in solids: Assessment of the Heyd-Scuseria-Ernzerhof screened Coulomb hybrid functional. *J. Chem. Phys.* **2004**, *121*, 1187−1192.
(36) Mosquera-Lois, I.; Kavanagh, S. R.; Walsh, A.; Scanlon, D. O. Navigating the defect configurational landscape. *J. Open Source Software* **2022**, *7*, No. 4817.
(37) Mosquera-Lois, I.; Kavanagh, S. R.; Walsh, A.; Scanlon, D. O. Identifying the ground state structures of point defects in solids. *npj Comput. Mater.* **2023**, *9*, No. 25.
(38) Stoffel, R. P.; Wessel, C.; Lumey, M.-W.; Dronskowski, R. Ab initio thermochemistry of solid-state materials. *Angew. Chem.* **2010**, *49*, 5242−5266.
(39) Jackson, A. J.; Walsh, A. Oxidation of GaN: An ab initio thermodynamic approach. *Phys. Rev. B* **2013**, *88*, No. 165201.
(40) Tolborg, K.; Klarbring, J.; Ganose, A. M.; Walsh, A. Free energy predictions for crystal stability and synthesisability. *Digital Discovery* **2022**, *1*, 586−595.
(41) Jackson, A. J.; Walsh, A. Ab initio thermodynamic model of Cu2ZnSnS4. *J. Mater. Chem. A* **2014**, *2*, 7829−7836.
(42) Gross, N.; Sun, Y.-Y.; Perera, S.; Hui, H.; Wei, X.; Zhang, S.; Zeng, H.; Weinstein, B. A. Stability and Band-Gap Tuning of the Chalcogenide Perovskite $BaZrS_3$ in Raman and Optical Investigations at High Pressures. *Phys. Rev. Appl.* **2017**, *8*, No. 044014.
(43) Espinosa, M. R.; Ertem, M. Z.; Barakat, M.; Bruch, Q. J.; Deziel, A. P.; Elsby, M. R.; Hasanayn, F.; Hazari, N.; Miller, A. J. M.; Pecoraro, M. V.; et al. Correlating Thermodynamic and Kinetic Hydricities of Rhenium Hydrides. *J. Am. Chem. Soc.* **2022**, *144*, 17939−17954.
(44) Kavanagh, S. R.; Squires, A. G.; Nicolson, A.; Mosquera-Lois, I.; Ganose, A. M.; Zhu, B.; Brlec, K.; Walsh, A.; Scanlon, D. O. doped: Python toolkit for robust and repeatable charged defect supercell calculations. *J. Open Source Software* **2024**, *9*, No. 6433.
(45) Wang, X.; Kavanagh, S. R.; Walsh, A. Sulfur Vacancies Limit the Open-Circuit Voltage of Sb2S3 Solar Cells. *ACS Energy Lett.* **2025**, *10*, 161−167.
(46) Yuan, Z.; Dahliah, D.; Claes, R.; Pike, A.; Fenning, D. P.; Rignanese, G.-M.; Hautier, G. Assessing Carrier Mobility, Dopability, and Defect Tolerance in the Chalcogenide Perovskite $BaZrS_3$. *PRX Energy* **2024**, *3*, No. 033008.
(47) Kumagai, Y.; Oba, F. Electrostatics-based finite-size corrections for first-principles point defect calculations. *Phys. Rev. B* **2014**, *89*, No. 195205.
(48) Aggarwal, G.; Mirza, A. S.; Riva, S.; Comparotto, C.; Frost, R. J. W.; Mukherjee, S.; Morales-Masis, M.; Rensmo, H.; Scragg, J. S. Charge Transport and Defects in Sulfur-Deficient Chalcogenide Perovskite $BaZrS_3$. *PRX Energy* **2025**, *4*, No. 033001.
(49) Yang, L.; Liu, T.; Jiang, J.; Song, W. Thermodynamics of native defects in Li2O: A first-principles study. *J. Solid State Chem.* **2023**, *322*, No. 123933.
(50) Lee, J.; Han, S. Thermodynamics of native point defects in a-Fe2O3: an ab initio study. *Phys. Chem. Chem. Phys.* **2013**, *15*, 18906−18914.

https://doi.org/10.1021/acs.jpcc.5c00828
J. Phys. Chem. C 2025, 129, 19473−19479